

Simulation of Estuarine Flooding and Dewatering with Application to Great Bay, New Hampshire

J. T. C. Ip^a, D. R. Lynch^a and C. T. Friedrichs^b

^aDartmouth College, Hanover, New Hampshire, 03755, U.S.A.

^bCollege of William and Mary, Gloucester Point, Virginia, 23062, U.S.A.

Received 30 September 1996 and accepted in revised form 18 February 1998

A finite element model for simulating tidal flooding and dewatering of shallow estuaries is described and applications to hypothetical embayments and to the Great Bay, New Hampshire estuary system, are presented. The model incorporates two-dimensional kinematic wave physics, with a porous medium beneath the open channel to incorporate the realistic drainage of dry elements on a fixed, high resolution mesh. The Galerkin method is used on simple linear finite elements and solved implicitly with iteration in time.

Simulations of idealized channels conserve mass, display physically correct behaviour, and agree with applicable one-dimensional results. Solutions for Great Bay further illustrate the physics of tidal flat hydrodynamics, characteristic distributions of bottom shear stress and the influence of topography on the overall circulation in the region. Sediment transport implications are discussed.

© 1998 Academic Press

Keywords: tidal estuaries; simulation; tidal flats; tidal currents; tidal friction; morphology; sediment transport

Introduction

Much of the world's open coasts are interrupted by inlets to bays, estuaries and lagoons. Most of these numerous and widespread embayments have length scales on the order of 10 km and depths of a few metres average which is comparable to the tidal range. These shallow, small-scale embayments are critical parts of coastal ecosystems. They are strongly non-linear, and generate significant distortion of the

surface tide as it propagates through. The resulting distortion of the velocity and bottom-stress time series is of major significance to sediment transport and accumulation.

TABLE 1. Governing equations in both the open channel and the porous medium for the uniform porous medium case of Figure 1

Saturated region, $H > h_0$	Unsaturated region, $H < h_0$
$q_p = -\kappa h_0 \nabla \zeta$	$q_p = -\kappa H \nabla \zeta$
$q_o = -(H - h_0)^{3/2} \sqrt{\frac{g}{c_d \nabla \zeta }} \nabla \zeta$	$q_o = 0$
$q = q_o + q_p = -D \nabla \zeta$	$q = q_p = -D \nabla \zeta$
$D = \kappa h_0 + (H - h_0)^{3/2} \sqrt{\frac{g}{c_d \nabla \zeta }}$	$D = \kappa H$
$v_o = \frac{q_o}{H - h_0}$	$v_o = 0$
$v_p = \frac{1}{\varepsilon} \frac{q_p}{h_0}$	$v_p = \frac{1}{\varepsilon} \frac{q_p}{H}$
$S = 1$	$S = \varepsilon$

κ is the hydraulic conductivity for the porous medium, $H = h + h_0 + \zeta$ is the total depth of the water column, h_0 is the thickness of the porous medium and ε is the porosity of the porous medium. v_o and v_p are the vertically averaged velocities in the open channel and porous medium, respectively.

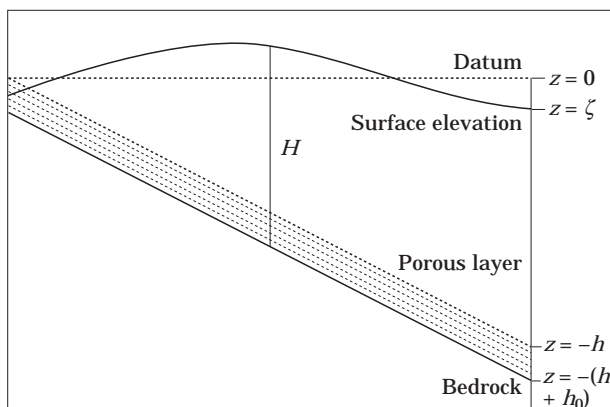


FIGURE 1. Schematic geometry for the flooding and dewatering model. ζ , surface elevation; h , bathymetric depth; h_0 , thickness of the porous medium.

TABLE 2. Simulation parameters for M_2 tidal flow in embayments, rch0, rch6 and rch9

Description	Parameters
x -Dimension	$0 \leq x \leq 3$ km
y -Dimension	$-1.5 \text{ km} \leq y \leq 1.5$ km
Grid spacing $\Delta\delta=75$ m	
Bathymetry range	$0 \leq h \leq 3$ m
Porous layer thickness	$h_0=0.25$ m
Hydraulic conductivity	$\kappa=3.162 \times 10^{-4}$
Drag coefficient	$c_d=0.005$
Time increment	$\Delta t=111.78$ s
Time steps per tidal period	400
Tidal periodicity	$T=12.42$ h
Length of simulation	$0 \leq t \leq 6T$
Numerical implicitity	$\theta=1$
Number of non-linear iterations	5

The strong hydrodynamic non-linearities and the important interactions between circulation, sediment transport and morphology have posed difficult scientific problems which remain beyond our mathematical abilities. Here the authors shall address these questions using advanced numerical modelling, focusing on circulation and morphological interactions in terms of topography, tidal hydrodynamics and characteristic distributions of bottom shear stress. Application of the finite element method in particular, provides a powerful tool in aiding the understanding of tidal-flat physics due to gridding flexibility in resolving complex coastal features.

The modelling of flooding and dewatering of shallow embayments presents special mathematical difficulties, as the domain of simulation must evolve in response to the computed solution itself. Past attempts to deal with these processes can be broadly described in two categories: (1) models with a spatially deforming computational grid; and (2) models with a spatially fixed computational grid. The most widely used approach to flooding and dewatering processes in operational hydrodynamic models assumes a fixed-boundary computational grid. These use the logical switching of entire grid cells (finite difference methods) or elements (finite element methods) between active (wet) and passive (dry) states depending on the computed elevation. At selected time intervals an assessment is made of whether additional areas in the grid have become active or passive. This approach has been implemented in the earliest operational models (e.g. Leendertse, 1970). In its simplest form, areas are restricted to filling or draining in whole grid increments (e.g. Reid & Bodine, 1968; Flather &

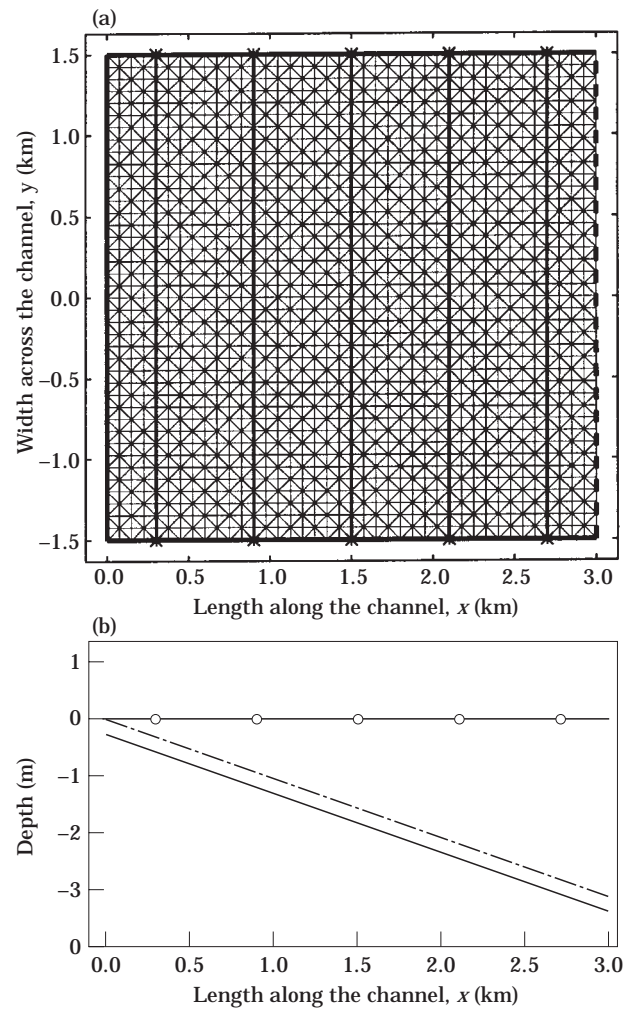


FIGURE 2. (a) The finite element computational grid, rch0 (1681 nodes, 3200 elements). The five vertical lines mark the five transect cuts. The dashed line marks the seaward M_2 tidal forcing boundary. (b) The side view of the uniformly sloping bathymetry running parallel along the channel. The dot-dashed line is the top of the porous medium. The \circ marks the location of the time-series record.

Heaps, 1975; Yeh & Chou, 1979; Leendertse, 1987; Thomas *et al.*, 1990; Yu *et al.*, 1990; Cialone, 1991; Jelesnianski *et al.*, 1992; Hervouet & Janin, 1994), although efforts have also been made to wet and dry more gradually. The latter is generally accomplished by modifying the governing equations to include some type of cell or element 'size factor' that varies from 0 to 1 as a function of water depth. Examples of this include the 'marsh porosity method' used by Thomas *et al.*, (1990) and similar techniques by Flather and Hubbert (1990) and Defina *et al.* (1994). In addition to flooding and dewatering in whole or fractional grid increments, there are fixed-grid

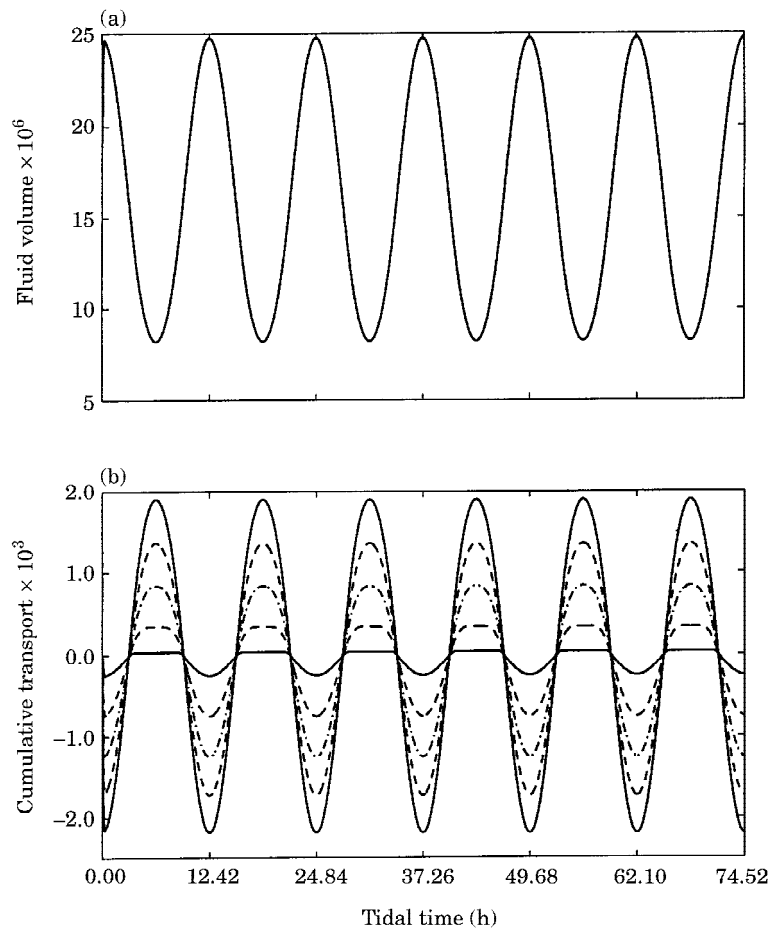


FIGURE 3. Time series of the total fluid volume (a) and the cumulative transport across the five transects (b) for the rch0 grid. The periodic solid line with the most variation in one cycle corresponds to the seaward transect at $x=2.7$ km; that with the least variation, the landward transect; etc.

algorithms which can differ in the basic governing equations used to represent the flooding and drying process. An example is the WIFM model (Leenknecht *et al.*, 1984; Vemulakonda, 1988; Cialone, 1991), in which weir-type relationships govern the filling and draining of boundary cells. Other models use the long-wave equations, often without the advective terms included (Reid & Bodine, 1968; Leendertse, 1987; Thomas *et al.*, 1990; Jelesnianski *et al.*, 1992). Several operational models allow for the possibility of subgrid scale barriers by using weir formulae in place of, or in combination with, the long-wave equations when these features are encountered (Leendertse, 1987; Jelesnianski *et al.*, 1992). Most recently, Luettich and Westerink (1995a; 1995b) have implemented these ideas on finite elements, by assuming the existence of removable barriers along the sides of all elements. They have obtained stable and reasonably realistic solutions, but with oscillations when elements turned on during flood.

The most precise computational approach is treatment as a moving boundary problem with front-tracking. This strategy essentially requires the computational grid to deform as the simulation proceeds, such that mesh boundaries always conform to the transient position of the shore (defined by the moving boundary conditions of zero total depth, zero normal transport and finite normal velocity). The finite element method is naturally suited to this mathematical approach. At every time step, the water level, the horizontal velocity and the position of the grid is recomputed. Early formulations and experiments in shallow water (Sielecki & Wurtele, 1970; Lynch & Gray, 1980) showed the promise of this deforming grid strategy. Although this approach is conceptually attractive, in practice it can lead to highly deformed grids, and has the additional computational requirement of continuous mesh adjustment and regeneration—a significant burden in practical situations. Consequently, it has primarily been restricted

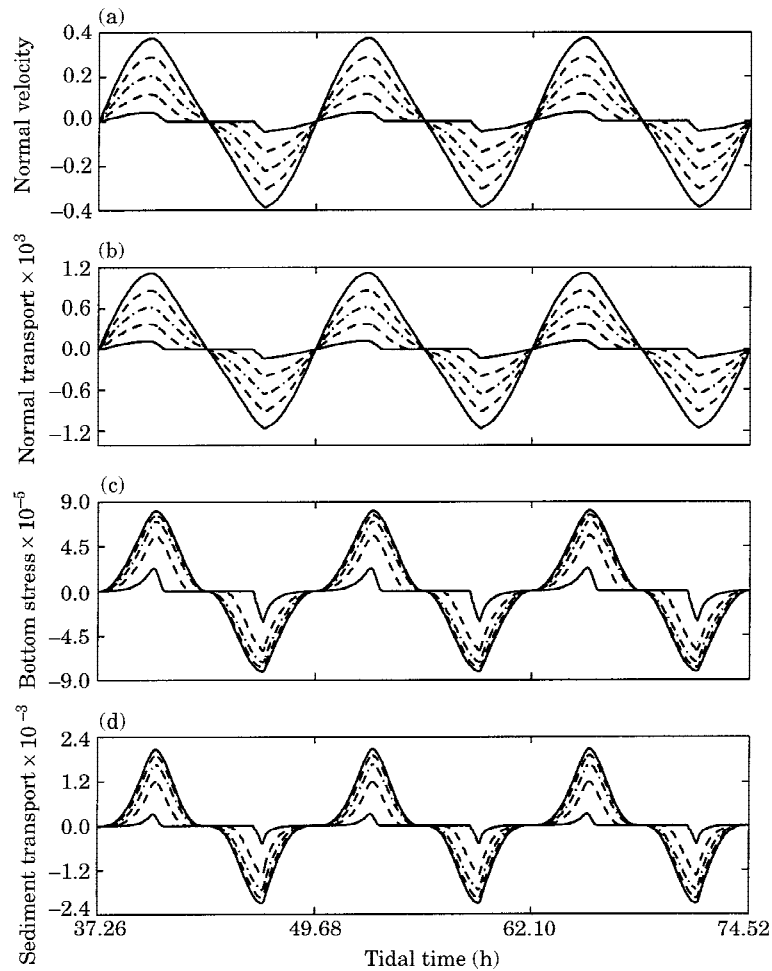


FIGURE 4. Time series of the velocity (a), transport (b), bottom stress (c) and sediment transport (d) all at $y=0$ normal to the five transects during the second half of the *rch0* simulation (three M_2 periods). The periodic solid line with the most variation in one cycle corresponds to the seaward transect; that with the least variation, the landward transect; etc.

to applications involving idealized test problems (e.g. Akanbi & Katapodes, 1988; Sidén & Lynch, 1988; Austria & Aldama, 1990). In the present work, the authors opt for a high resolution, fixed-mesh approach, with finite elements the natural choice in order to facilitate variable local resolution.

Another critical modelling issue is the level of physical representation. The hydrodynamics are well-described by the classical two-dimensional shallow-water equations. However small length scales, combined with near-critical flow conditions as the depth approaches zero, conspire to make the control of advection the dominant *computational* theme, even when other processes are physically dominant. Scale analysis and numerical simulation (Friedrichs *et al.*, 1992; Friedrichs & Madsen, 1992) as well as field observation (Swift & Brown, 1983) indicate that the primary force balance is between friction and the

pressure gradient in shallow tidal embayments. It is practical in these circumstances to adopt a momentum equation reduced to this simple balance, thereby eliminating the unneeded complications of the acceleration terms. The authors refer to this as the 'kinematic' approximation. Fixed-boundary kinematic equations have been explored in river routing (Lighthill & Whitham, 1955; Katapodes, 1984), overland flow (Wooding, 1965; USACE, 1981; Liong *et al.*, 1989), irrigation (Strelkoff & Katapodes, 1977; Katapodes, 1982), tsunami propagation (Murty, 1983) and, to some extent, in tidal estuaries (LeBlond, 1978). Their potential in the small-scale estuarine context merits further development. This is the approach adopted herein.

A final simulation issue concerns the representation of the flow regime at very low water levels. Conventional practice is to deactivate entire elements when

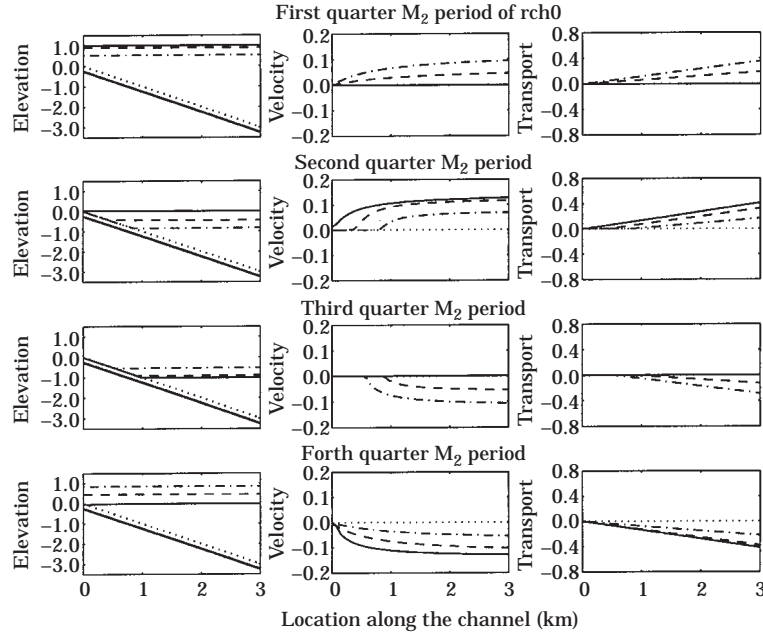


FIGURE 5. Time series of the surface elevations, velocities and transports for each of the four quarters of a M_2 tidal cycle along a transect down the centre of the channel. In the first figure of each panel (elevation), the thicker solid line and the dotted line represent the bedrock and the top of the porous layer respectively. In all the figures, the solid line represents the beginning of each quarter cycle of a 400 steps period, i.e. at time step 0, 100, 200 and 300, respectively in each of the quarter panels. The dashed line and the dot-dashed line represent subsequently 30 and 65 time-steps behind the beginning of each quarter cycle. In the second and third figures of each panel (velocity and transport), the dotted lines are the y -velocity and transport, indistinguishable from 0.

they are sufficiently dry. The authors seek to represent the continuous, slow drainage via subgrid-scale roughness, vegetation and drainage networks, and unconsolidated sediment. All of these may be represented as a heterogeneous porous medium underlying the conventional water column, and this is explored herein.

Summarizing, the computational design requirements call for a continuously evolving shoreline geometry; fine resolution of landform and local bathymetry; and open-channel hydrodynamics which approach those of a porous medium at low water levels. Operational simplicity demands a fixed-grid approach, variable local resolution and an algorithm which is not dominated by numerical control of advection in situations where it is unimportant.

These requirements lead to the finite element model described below.

Two-dimensional kinematic model

The authors start with the two-dimensional depth-averaged equations. Systems considered here are small enough to neglect Coriolis accelerations, and

vertically-mixed so their dynamics may be treated adequately by depth-integrated models. For the limiting case with a smooth, impermeable substrate:

Continuity:

$$\frac{\partial H}{\partial t} + \nabla \cdot H\mathbf{v} = 0 \quad (1)$$

Horizontal momentum:

$$\frac{\partial \mathbf{v}}{\partial t} + \mathbf{v} \cdot \nabla \mathbf{v} + \mathbf{g} \nabla \zeta + \frac{c_d}{H} |\mathbf{v}| \mathbf{v} = 0 \quad (2)$$

where \mathbf{v} is the depth-averaged velocity, t is time, ∇ is the horizontal gradient differential operator, ζ is the surface elevation relative to a horizontal datum, \mathbf{g} is the acceleration of gravity, c_d is the bottom drag coefficient, $H = h + \zeta$ is the total depth of the water column and h is the bathymetric depth.

The authors follow the kinematic reduction of these equations. Recognizing the primary balance between friction and the pressure gradient in shallow tidal embayments, the momentum balance becomes:

$$\mathbf{g} \nabla \zeta + \frac{c_d}{H} |\mathbf{v}| \mathbf{v} = 0 \quad (3)$$

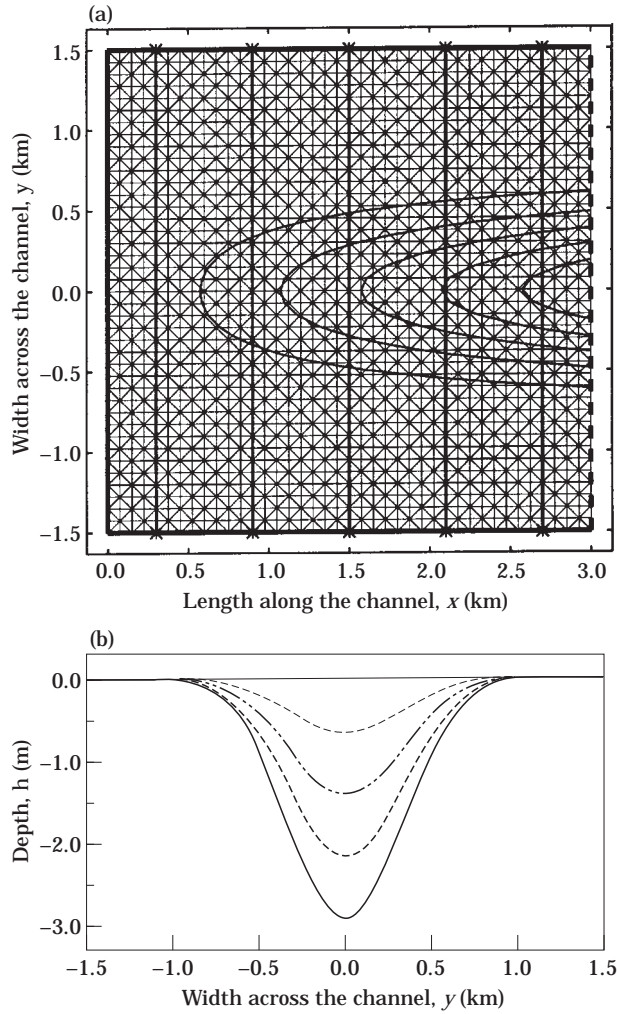


FIGURE 6. (a) The finite element computational grid, rch6 (1681 nodes, 3200 elements). The five vertical lines mark the five transect cuts and the contour lines are the bathymetry (0.5 m–2.5 m). (b) The cross-section of the depth profile across the channel at five equally spaced locations along the length starting from land at $x=0$ (thin line) to sea at $x=3$ km (thick line). These depths represent the top of the porous medium at the location.

Following Friedrichs *et al.* (1992), this is rearranged to obtain the transport $q \equiv Hv$ as follows:

$$q = -\sqrt{\frac{gH^3}{c_d|\nabla\zeta|}} \nabla\zeta \quad (4)$$

Equation 4 is then substituted into the continuity Equation 1 to obtain the kinematic equation:

$$\frac{\partial\zeta}{\partial t} - \nabla \cdot D\nabla\zeta = 0 \quad (5)$$

with non-linear diffusion coefficient D :

$$D = H \sqrt{\frac{gH}{c_d|\nabla\zeta|}} \quad (6)$$

This equation was solved in one-dimension by Friedrichs *et al.* (1992). Therein, the basic numerical approach (i.e. a non-linear diffusion computation) was shown to be practical, and comparisons with numerical solutions of the full dynamic equations of motion confirmed the validity of the simpler kinematic equations for these length and time scales.

This basic idea is extended by adding a porous layer beneath the open channel. This feature allows a natural transition, as the water level is lowered, from pure open-channel flow to a Darcian description of subgrid-scale topographic variations, vegetation and drainage patterns, etc. and ultimately to an impermeable substrate. This is achieved by specification of the variation of the porosity and hydraulic conductivity of the medium as a function of depth. The result is that 'dry' areas continue to participate hydraulically in the overall system, and the free surface is allowed to fall below the usual bathymetric depth in a natural way. The combined open-channel and porous medium system is described by a generalization of Equations 4–6:

$$q = q_o + q_p = -D\nabla\zeta \quad (7)$$

$$S \frac{\partial\zeta}{\partial t} + \nabla \cdot q = 0 \quad (8)$$

wherein q_o is the transport in the open channel as above Equation 4; q_p is the porous medium transport, described by Darcy's law; and D and the storage coefficient S are specified as functions of ζ and z . Elimination of q gives us the non-linear diffusion equation:

$$S \frac{\partial\zeta}{\partial t} - \nabla \cdot D\nabla\zeta = 0 \quad (9)$$

In the present tests, an idealized, abrupt transition to a uniform porous medium is used as shown in Figure 1. The relevant flow laws and parameter values listed in Table 1.

This non-linear diffusion Equation 9 is discretized on linear finite elements by the Galerkin method in space. Conventional, implicit finite differences are applied in time:

$$S^{k+\theta} \left[\frac{\zeta^{k+1} - \zeta^k}{\Delta t} \right] - \nabla \cdot D^{k+\theta} \nabla [\theta \zeta^{k+1} + (1-\theta) \zeta^k] = 0 \quad (10)$$

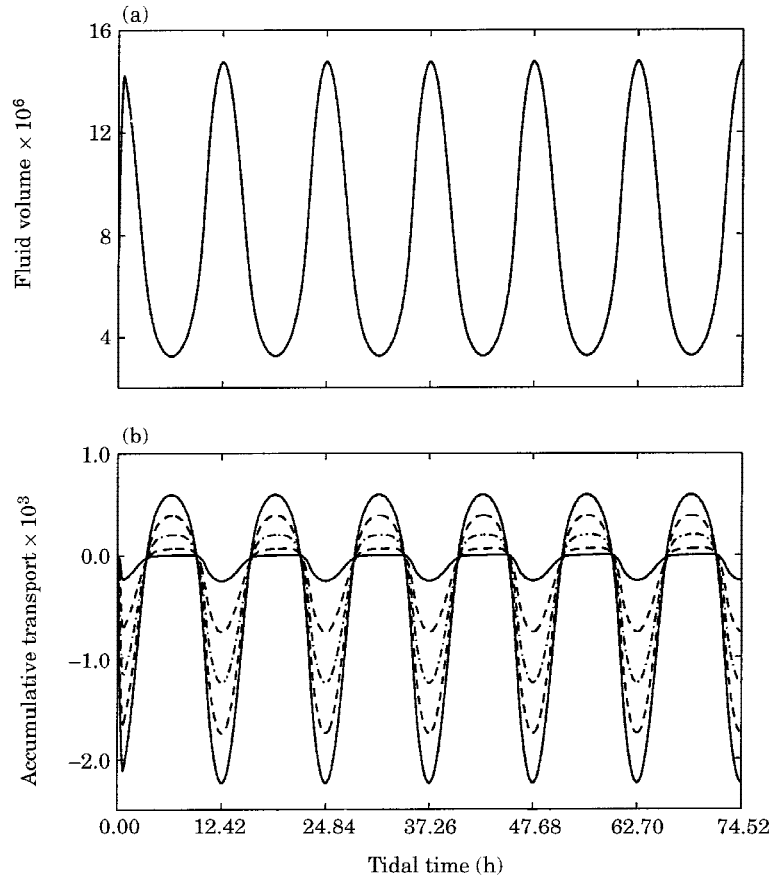


FIGURE 7. Time series of the total fluid volume (a) and the cumulative transport across the five transects (b) for the rch6 grid. The convention is the same as in Figure 3.

and solution is obtained iteratively in each time step.

Test problems: embayment with analytical bathymetries

The model has been tested in the following three example problems. All these example problems consist of tidal flow in a 3 by 3 km square embayment [see (a) in Figures 2, 6, and 12] with a linearly sloping bathymetry running along the channel length (z -direction) but with different depth profiles across the channel [see (b) In Figures 2, 6, and 12]. The landward boundary is at $x=0$ with zero depth and the seaward boundary is at $x=3$ km with maximum depth of 3 m. The system is forced with a simple M_2 tide:

$$\zeta = \cos\left(\frac{2\pi t}{T}\right) \quad (11)$$

at the seaward boundary. In boundary condition Equation 11, ζ (units of metres) is the elevation, t and

T are the time and the M_2 period (12.42h) in seconds respectively. All the simulation parameters are summarized in Table 2. Every simulation was started with fluid at rest and was terminated after six M_2 tidal cycles at dynamic equilibrium, in which solutions were periodic.

Uniformly sloping bathymetry (rch0)

This first problem consists of a simulated tidal flow in a channel with a linearly sloping bottom with uniform depth across the width of the channel. This is essentially a one-dimensional case. The Figure 2 (a) illustrates the computational grid, named rch0, which consists of 1681 nodes and 3200 linear triangular elements in equilateral union-jack configuration. The spatial grid spacings are identical along both the x - and y -direction with $\Delta\delta=75$ m. Figure 2 (b) shows the side view of the sloping bottom topography running parallel along the channel.

The results are displayed in Figures 3–5. Figure 3 shows the complete time history of the total fluid

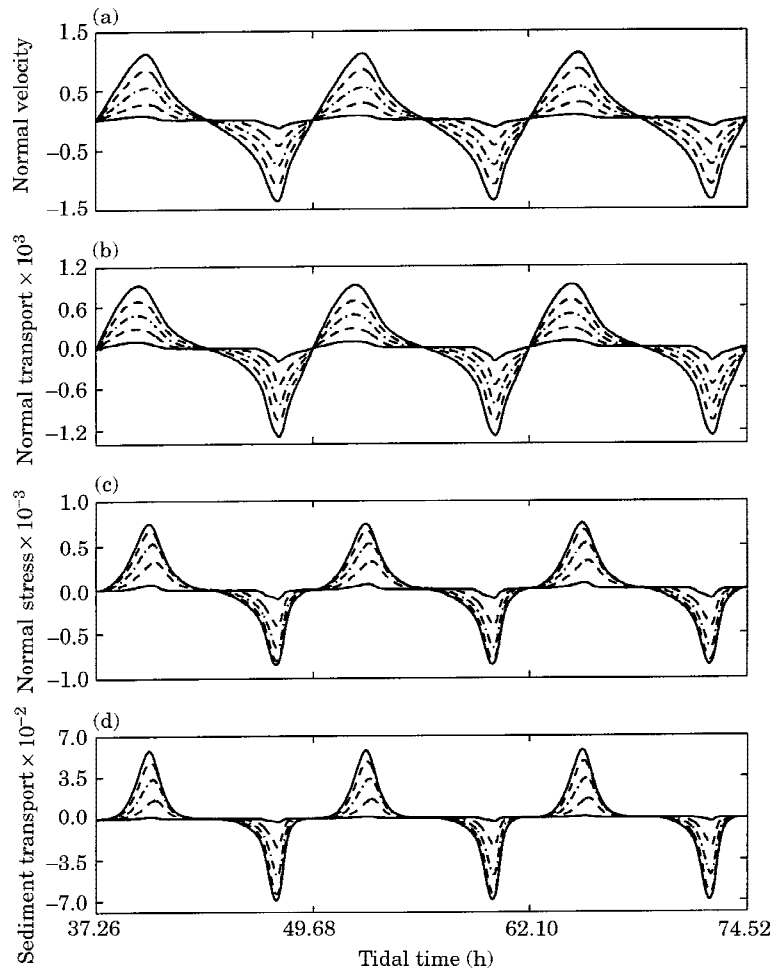


FIGURE 8. Time series of the normal velocity (a), transport across the five transects (b), normal bottom stress (c), and normal sediment transport (d) in the centre of the channel during the second half of the *rch6* simulation (four M_2 periods). The convention is the same as in Figure 4.

volume ($\iint H \, dx \, dy$) and the cumulative transport ($\int_0^t \int q_x \, dy \, dt$) across the five transects as shown in Figure 2. The two figures conclusively illustrate the system has reached a dynamic equilibrium and mass conservation is maintained during the simulation after the initial tidal cycle.

Figure 4 shows the time series of velocity ($\mathbf{v} \cdot \mathbf{e}_x$), transport ($\int q_x \, dy$), bottom stress ($c_d |\mathbf{v}| \mathbf{v} \cdot \mathbf{e}_x$), and sediment transport ($|\mathbf{v}|^2 \mathbf{v} \cdot \mathbf{e}_x$) normal to the five transects at the centre of the channel during the second half of the simulation. These results are almost identical to those obtained by using the earlier one-dimensional model (Friedrichs *et al.*, 1992).

Representative solutions of surface elevations, depth-average velocities and transports at 12 points in the tidal cycle sampled along the centreline of the channel, are presented in Figure 5. The wet/dry frontal interface migrates over a distance of approxi-

mately 1 km throughout a complete M_2 tidal period. At all times the solutions are quite smooth with no signs of any kind of oscillations or distress. It is evident that the present M_2 forcing induces a prolonged ebb phase at the landward end of the system, with shorter and stronger flood tide velocities. Results for the one-dimensional topography were virtually identical across the channel, with trivial y -component of velocity.

V-shaped bathymetry (rch6)

As a more demanding test case in true two-dimensional geometry, the second test case was performed on a square channel with sloping V-shaped bathymetry as shown in Figure 6. The simulation setup and the computational grid, named *rch6* (shown in the top panel of Figure 6) are identical to that of the

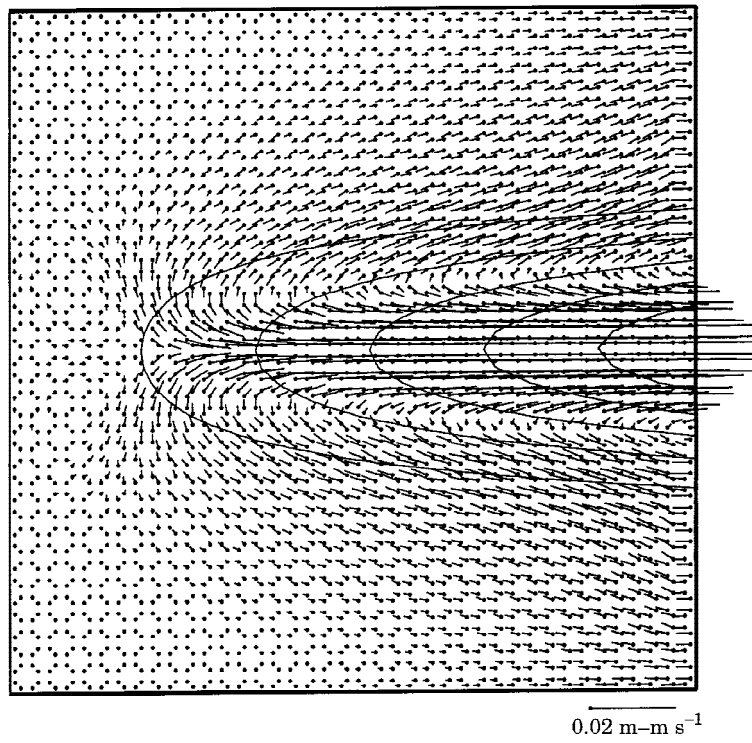


FIGURE 9. The panel displays the tidal time-averaged residual transport over a M_2 tidal cycle at dynamic equilibrium (rch6). The equally space contours show bathymetry increasing from 0.5 m at the outer contour to 2.5 m at the inner contour. The vectors are marked at their base and are drawn at the centroid of each element.

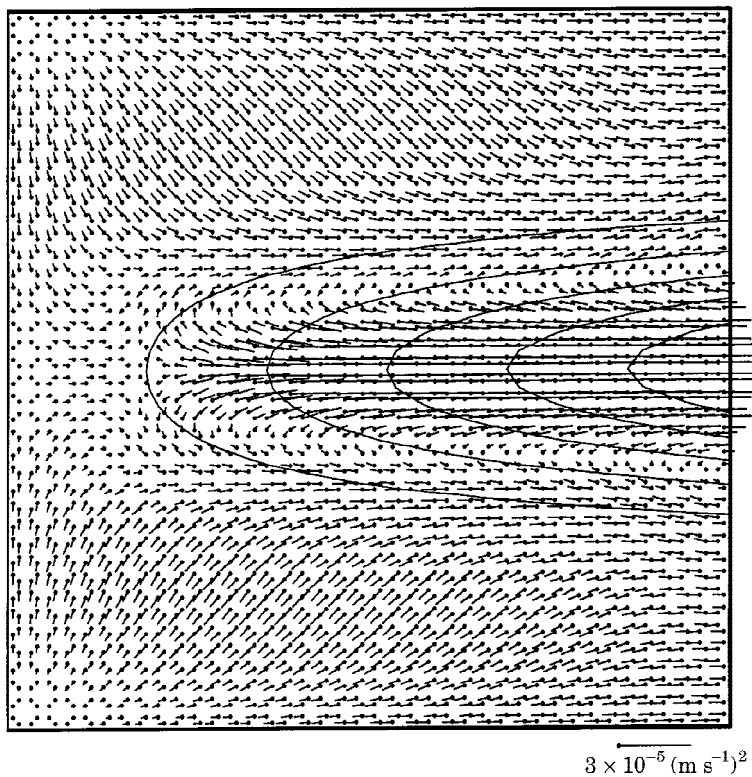


FIGURE 10. Residual bottom stress over a M_2 tidal cycle at dynamic equilibrium (rch6).

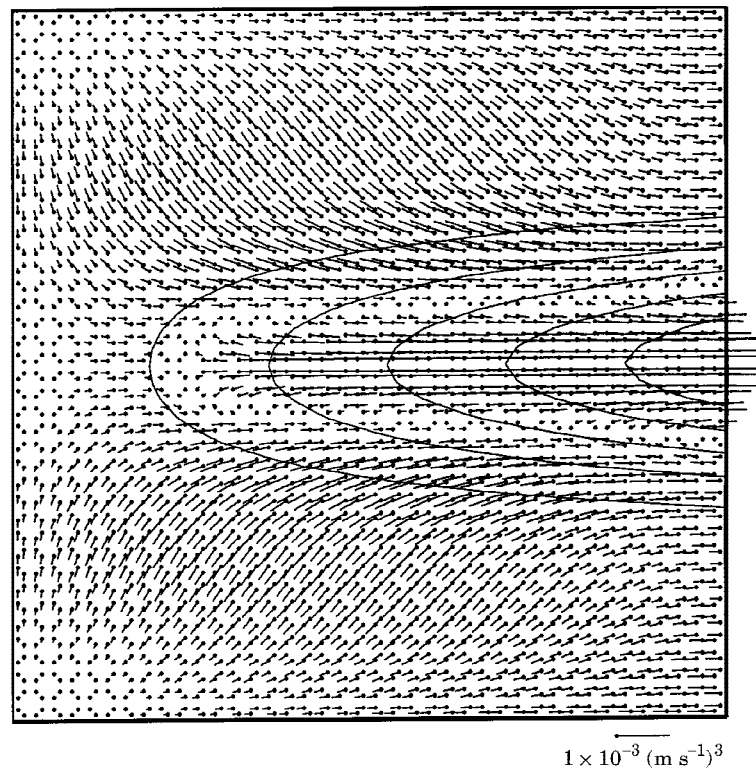


FIGURE 11. Residual sediment transport over a M_2 tidal cycle at dynamic equilibrium (rch6).

rch0 run described in the previous section; the only difference is the transverse bathymetry shown in the bottom panel of Figure 6.

Results are displayed in Figures 7–11. Figure 7 shows the full dynamic of the total fluid volume and the cumulative transport across the five transects as shown in Figure 6. As in the rch0 case, these figures conclusively illustrate the system has reached dynamic equilibrium with mass conservation after the initial tidal cycle, during which drainage occurs to accommodate the mean value of the boundary condition.

Figure 8 displays the partial time-series of the normal velocity, total transport across the cut, bottom stress and sediment transport along the centreline at the five transects, during the second half of the simulation. It is evident that the flood and ebb stages are highly asymmetric. The pattern with flood dominance at the landward end of the system, noted in rch0, is enhanced here.

Figure 9 shows the tidal time-averaged residual transport, Figure 10 the residual bottom stress, and Figure 11 the residual sediment transport over a M_2 period at dynamic equilibrium. The qualitative observation is that on average transport is directed inward at the shallower portions of the seaward forcing boundary then is turned around in the shallow interior

and is directed outward at the deep centre channel. The general tidal time-averaged bottom stress and sediment transport pattern are very similar with a shorewardly directed pattern at the shallow area and a seawardly directed pattern at the centre deep channel. These results are as expected and the solutions are perfectly symmetric and without any noticeable oscillation or distress.

Asymmetric W-shaped bathymetry (rch9)

As another rigorous test in two-dimension, a third test case was run on a square channel with sloping asymmetric W-shaped bathymetry as shown in Figure 12. The computational grid, named rch9 (shown in the top panel of Figure 12) is identical to the rch0 and the rch6 meshes except with an asymmetric W-shaped depth profile (shown in the bottom panel of Figure 12). The simulation setup is identical to those for rch0 and rch6.

After six M_2 cycles of simulation from a cold start, the analysed simulation results are displayed in Figures 13–19. Figure 13 shows the complete time history of the total fluid volume and the cumulative transport across the five transects as shown in Figure 12. As in the previous cases, dynamic equilibrium and mass conservation are confirmed

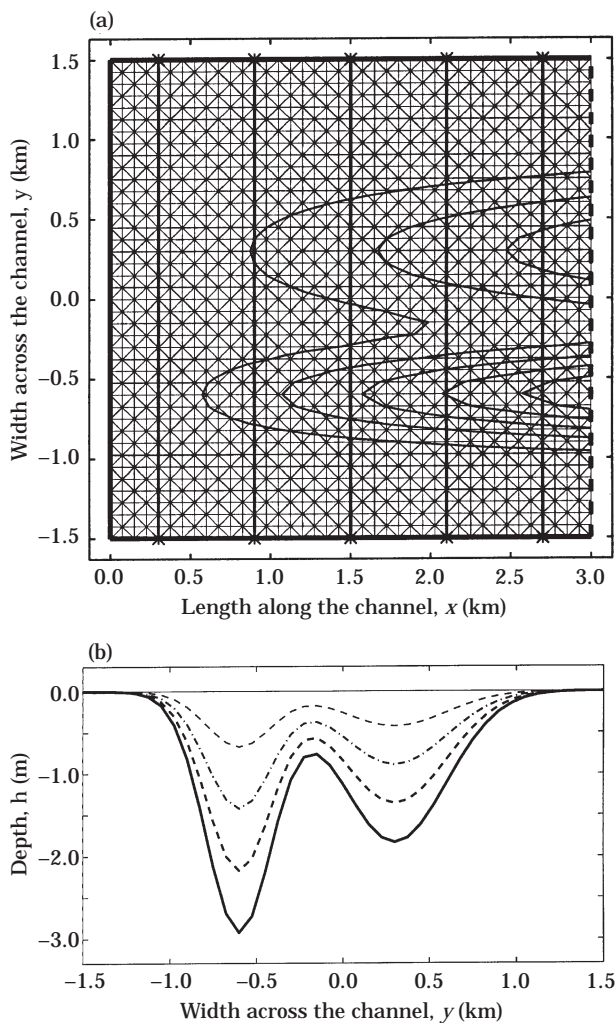


FIGURE 12. (a) The finite element computational grid, *rch9* (1681 nodes, 3200 elements). Bathymetric contours are at 0.5 m intervals. (b) The cross-section of the depth profile across the channel at five equally spaced locations along the length starting from land at $x=0$ (thin line) to sea at $x=3$ km (thick line). These depths represent the top of the porous medium at the location.

beginning in the second period. Figure 14 displays the time series of the maximum normal velocity, normal transport, maximum normal bottom stress and maximum normal sediment transport across the five transects during the second half of the simulation. As in the *rch0* and *rch6* runs, flood dominance in the shoreward transects is observed.

Figure 15 shows the time-averaged residual transport, Figure 16 the residual bottom stress, and Figure 17 the residual sediment transport over a M_2 period at dynamic equilibrium. The qualitative observation is that, on average, fluid is being transported in through the shallower portions of the seaward forcing boundary then is turned around in the shallow interior

and is being transported out at the two deeper centre channels. The transport is intensified at the shallower channel. The residual bottom stress and sediment transport show similar patterns of two oppositely directed intensified zones at the two deep channels and at the shallow flats. The simulation results exhibit behaviours of superposition of two side-by-side V-shaped channels. The solutions are smooth without any noticeable oscillation or distress, except for the slight wiggle near the 0.5 m isobath of the deep channel, which is due to resolution issue.

Figures 18 and 19 show the circulation patterns at maximum ebb at the end of the first quarter cycle and at maximum flood a third of the way into the final quarter cycle, respectively, within a M_2 tidal cycle after a dynamical equilibrium has been established. The transient solutions shown in this case are numerically well-behaved and appear to describe the realistic dynamics of the flooding and dewatering process in an asymmetric W-shaped channel with prescribed periodic M_2 tidal forcing across the sea boundary.

The Great Bay Estuary system

The Great Bay Estuary system (see Figure 20) is situated in south-eastern new Hampshire near the Durham and Newington areas, U.S.A. This estuary system has water exchange at the north through the Little Bay with the Oyster River and the Piscataqua River than to the Gulf of Maine, to the north-west the Crommet Creek, to the south-west the Lamprey River at Moodys point and Shackford point and the Squamscott River right below, to the south-east the Winnicut River below the Pierce Point. The Great Bay runs approximately 7 km from the Squamscott River south to Fox point in the north, and 7 km from the Lamprey River west to Swan Island in the east in the widest southern part of the embayment. It has a narrow upper channel approximately 0.5 km wide and of order 15 m deep running north to south from the Oyster River and the Piscataqua River inlet. The upper channel leads to a wide lower bay with tidal flats and mud flats in the order of a few metres deep near the shore boundaries. Flooding and dewatering is therefore important in determining the tidal circulation.

Computational grid and simulation setup

Dynamic analysis time series of current and sea-level measurements at a location near the middle strait shows that the principal force balance is between the frictional stress and the pressure gradient

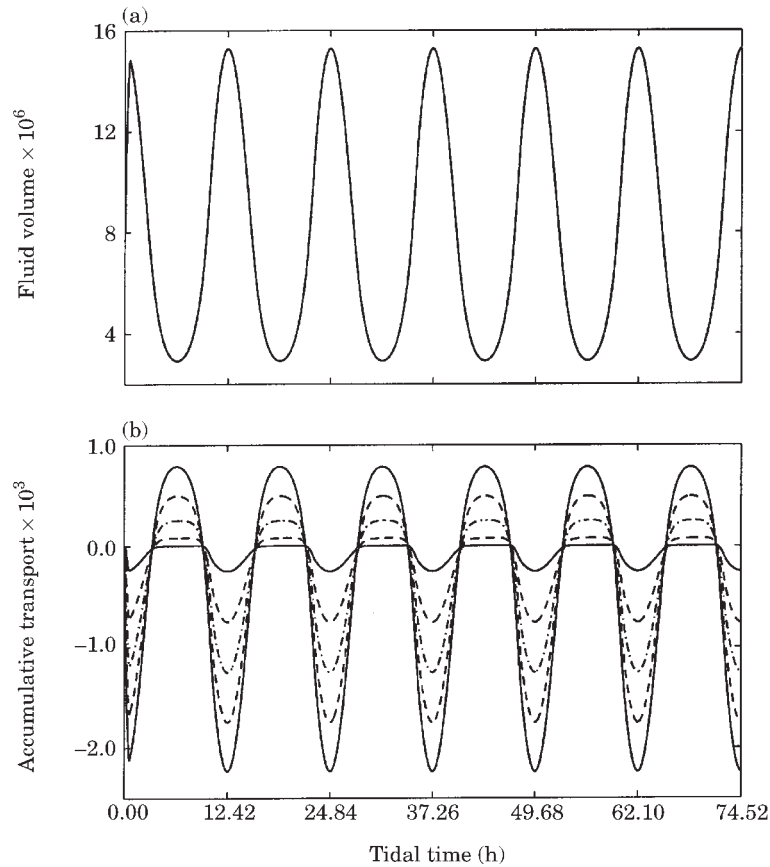


FIGURE 13. Time series of the total fluid volume (a) and the cumulative transport across the five transects (b) for the rch9 grid. The convention is the same as in Figure 3.

forcing (Swift & Brown, 1983). Hence, the kinematic assumption is confirmed. Figure 21 displays the computational grid, named gtb9 for the Great Bay Estuary system. The domain is discretized using linear equilateral triangles fitted to the boundary. There are 2861 nodes and 5185 elements with an average resolution of 50 m and a minimum grid spacing of no less than 25 m. The bathymetric contour lines shown in Figure 21 reveal a centre channel running north to south and tidal flats in the southern part of the domain.

M_2 tidal forcing is specified as a Dirichlet elevation boundary condition across the northern inlet boundary at the top (see Figure 21). The simulation setup is almost identical to the square channel runs reported above. All the simulation parameters are summarized in Table 3. The amplitude is 0.9 m (Swift & Brown, 1983). The stimulation was started with fluid at rest and was terminated after six M_2 tidal periods (approximately $t=75$ h). At the completion of the simulation, the results are analysed and are displayed in Figures 22–35.

Mass balance

Figure 22 shows the complete time history of the total fluid volume and the cumulative transport across the five transects as shown in Figure 21. As in the idealized cases, the system establishes a dynamic equilibrium rapidly, and mass conservation is thereafter maintained throughout the simulation after the initial tidal period.

Figure 23 displays the time series of maximum normal velocity, normal transport, maximum normal bottom stress and maximum normal sediment transport across the river transects during the second half of the simulation. The maximum normal velocity across the transects increases then decreases as one moves southward with the maximum level across the middle strait, while the normal transport across the same transects decreases to maintain mass conservation. Both quantities decrease sharply at the two tidal flat cuts. Similar to Figure 23, Figure 24 shows the results across the transects at the lower south-eastern tidal flats in zoom window no. 3. It

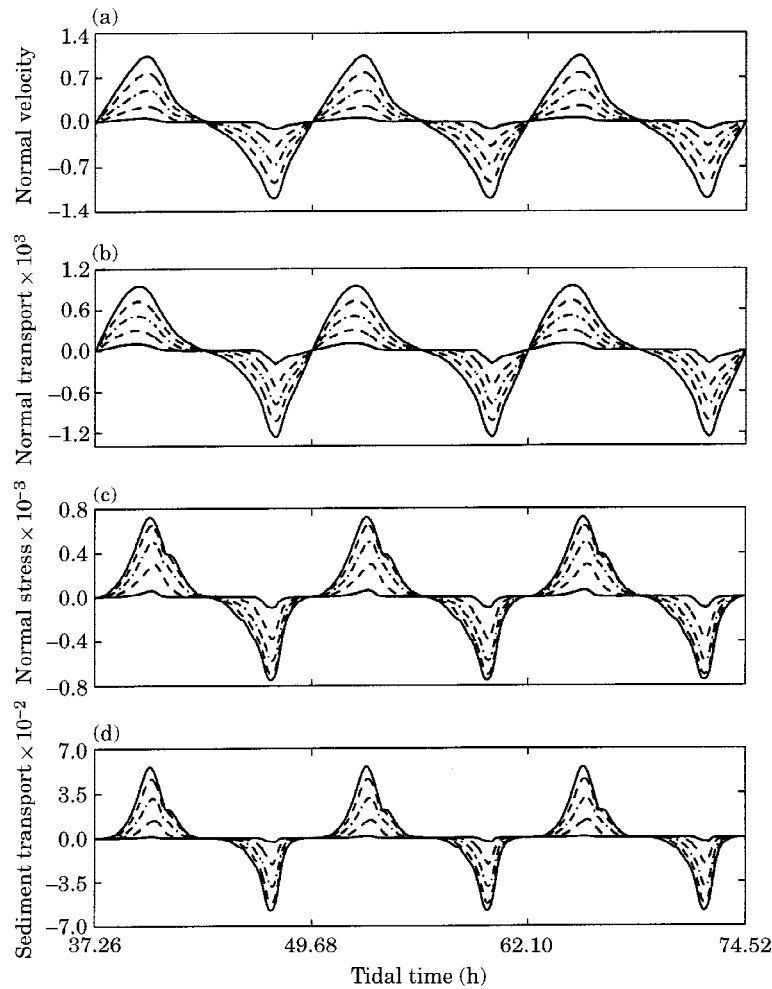


FIGURE 14. Time series of the normal velocity (a), transport across the five transects (b), normal bottom stress (c) and normal sediment transport (d) in the centre of the channel during the second half of the rch9 simulation (four M_2 periods). The convention is the same as in Figure 4.

is again noted that a certain asymmetry exists between flood and ebb, with the details distinctly different from those apparent in the idealized cases.

Residual analysis

Figures 25–27 show the detail pattern of the gtb9 residual transport for the upper channel (window no. 1), lower bay tidal flats (window no. 2) and lower eastern bay flats (window no. 3), respectively for the Great Bay Estuary system at dynamical equilibrium. The locations of the three zoom windows are given in Figure 21. As displayed in Figures 25–27, residual transport vectors are directed inward from the top inlet along the shore boundary and the shoreline tidal flats down the upper channel into the lower bay and

return outward through the deeper channel. Figure 25 shows there is a counter-clockwise gyre around a pit at the middle part of the channel just inside the inlet boundary. This causes residual transport out of the inlet at its middle portion. In general, residual transport vectors are pointing southward in the region outside the 5 m isobath in the northern channel and all the way through the narrow strait into the lower wide portion of Great Bay. The residual transport vectors return northward inside the 5 m narrow channel. This gives rise to a double gyres pattern which extends through the strait into the lower bay.

In Figure 26, it is observed that residual transport vectors are oriented south and south-westward above the 2.5 m isobath, then are oriented northward through the deeper channel. This creates several

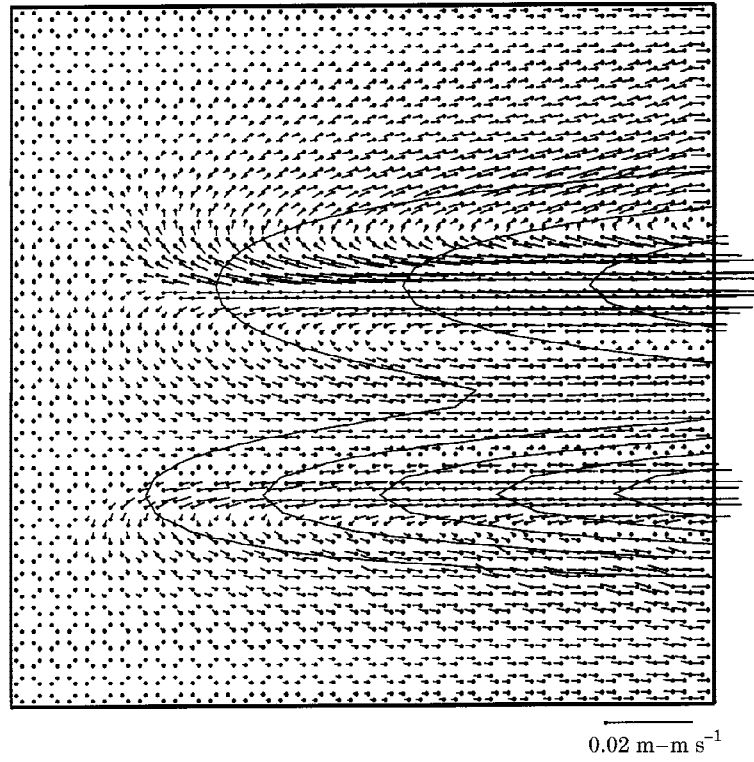


FIGURE 15. The panel displays the tidal time averaged residual transport over a M_2 tidal cycle at dynamic equilibrium (rch9). The equally spaced contours show bathymetry increasing from 0.5 m at the outer contour to 2.5 m at the inner contour. The vectors are marked at their base and are drawn at the centroid of each element.

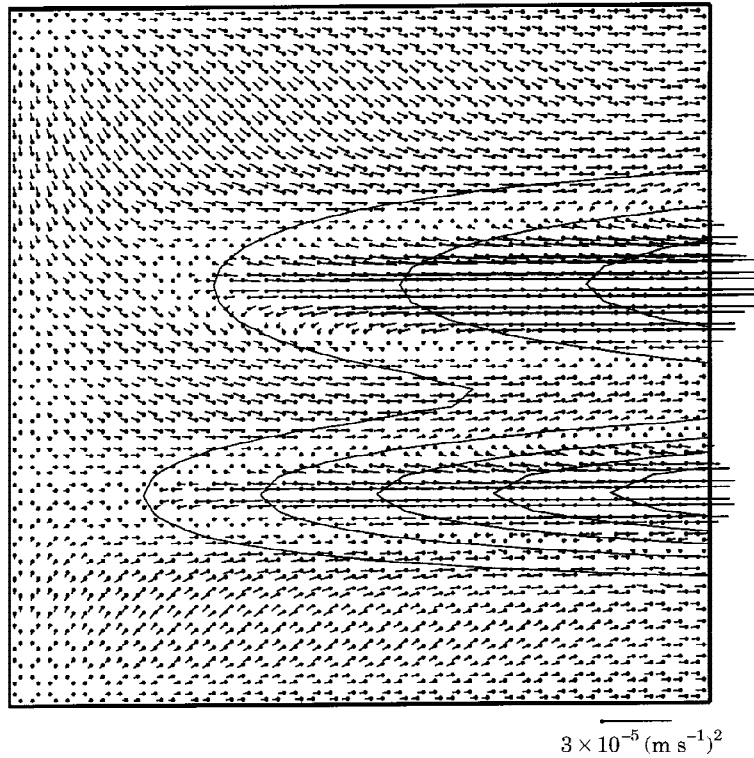


FIGURE 16. Residual bottom stress over a M_2 tidal cycle at dynamic equilibrium (rch9).

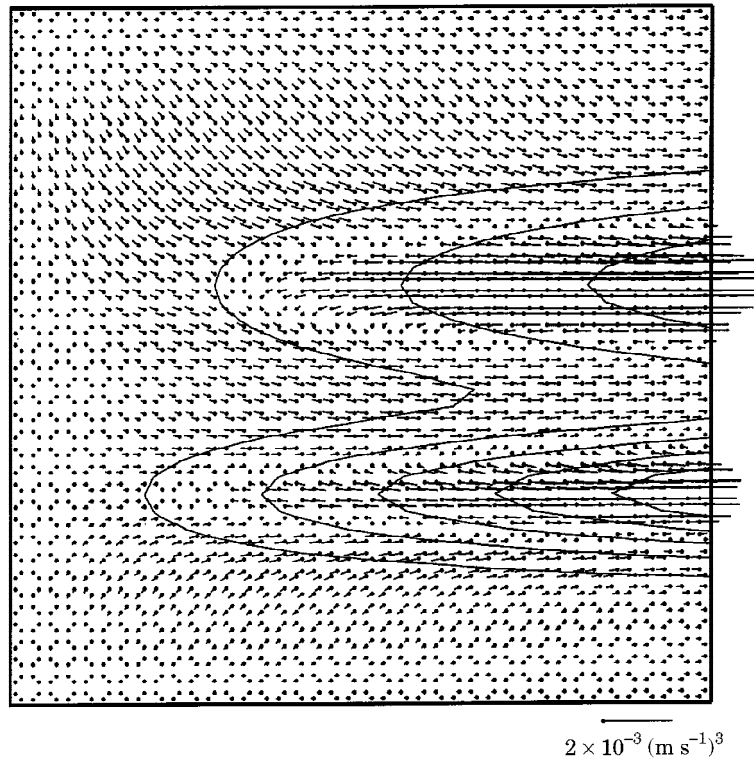


FIGURE 17. Residual sediment transport over a M_2 tidal cycle at dynamic equilibrium (rch9).

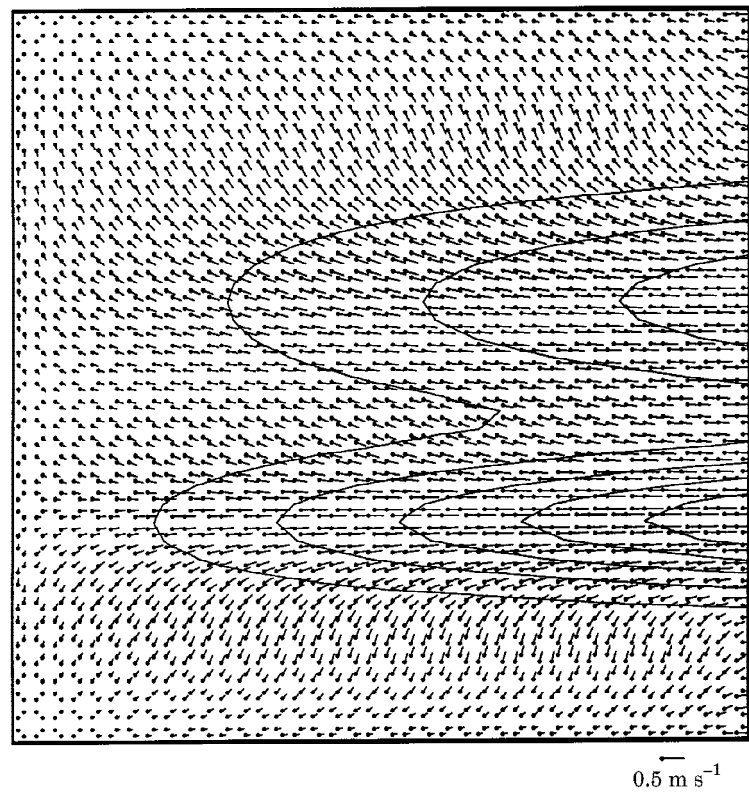


FIGURE 18. Circulation pattern of rch9 at maximum ebb at time step no. 95.

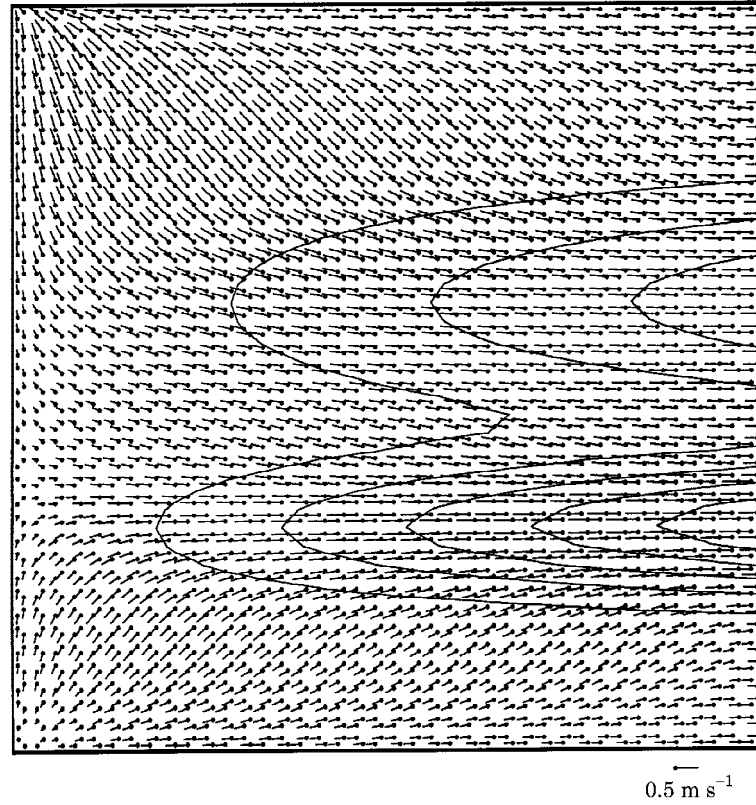


FIGURE 19. Circulation pattern of rch9 at maximum flood at time step no. 330.

circular patterns around the split deeper channel in the lower bay. It is also noticed that residual transport is stagnated around the rim 25 or 50 m away from the shoreline and most of the shallow eastern portion

of the tidal flats. Those areas are probably mostly dry during the cycle. Figure 27 shows in the eastern portion of the lower bay residual transport orients eastward along the two shores and forms a gyre in the middle to exit along the deeper channel. The disturbance in the gyre near the Winnicut River is due to closing off of the river and grid resolution and refinement problems.

Figures 28–30 illustrate the residual bottom stress pattern at dynamic equilibrium. The residual bottom stress, s is defined as:

$$s = \frac{1}{T} \int_0^T c_d |v| v dt \quad (12)$$

where v is the flow velocity and T is the period of the tide. It is observed that the residual bottom stress is intensified within the 2.5 m channel especially in the vicinity of the upper boundary inlet and the middle narrow strait.

Figures 31–33 reveal the residual sediment transport pattern. In this study, the residual sediment transport, t is defined as:

$$t = \frac{1}{T} \int_0^T |v|^2 v dt \quad (13)$$

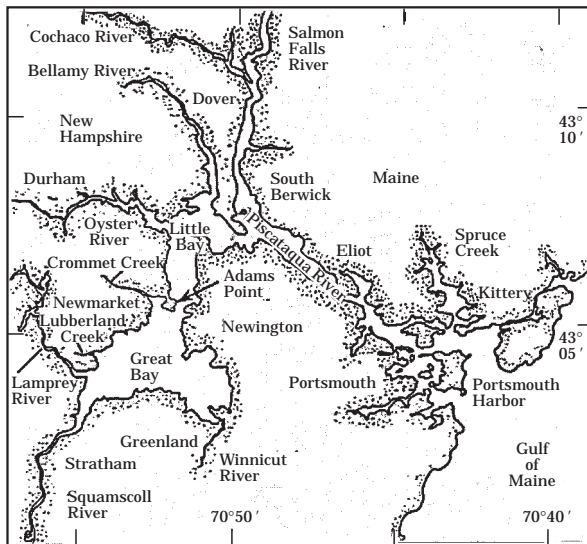


FIGURE 20. A map of the Great Bay Estuary system situated in south-eastern New Hampshire, U.S.A. (Short, 1992).

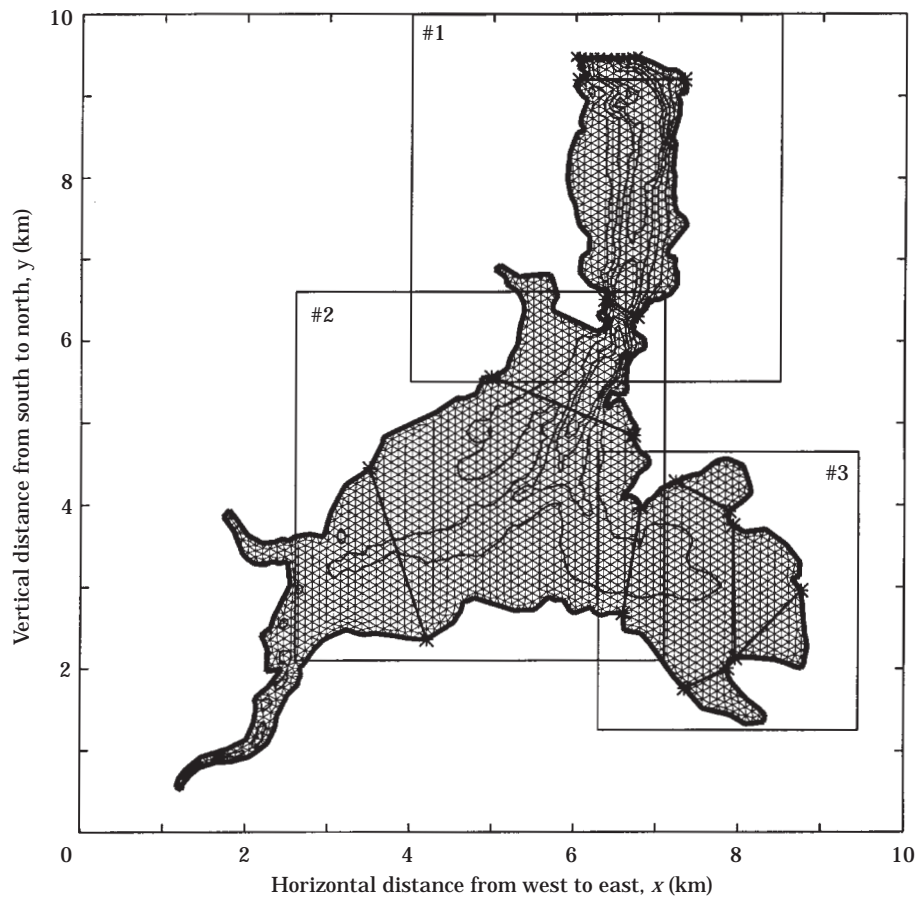


FIGURE 21. Finite element computational grid, gtb9 (2861 nodes, 5185 elements) of the Great Bay Estuary system. The five straight lines mark the five transect cuts. The northern top boundary marked by x is the inlet M_2 tidal forcing boundary. The 2.5, 5, 7.5 and 10 m bathymetric contours reveal a centre channel and tidal flats in the lower part. The square frames are the three zoom windows for residual data analysis.

With M_2 forcing, the residual sediment transport is observed to be the most intense near the narrow strait directed southward. The sediment transport is also

higher than the background level near all the river and bay inlets.

Transient solution

Figures 34 and 35 show the circulation patterns at maximum ebb at the end of the first quarter cycle and at maximum flood a fifth of the way into the final quarter cycle, respectively, within a M_2 tidal cycle after a dynamical equilibrium has been established. The transient solutions shown in this case are numerically well-behaved and appear to describe the realistic dynamics of the tidal flooding and dewatering process in this complex domain.

Summary

The authors have described and implemented a fixed-grid finite element equation based on the two-dimensional kinematic diffusion model with

TABLE 3. Simulation parameters for the Great Bay Estuary system New Hampshire, U.S.A.

Description	Parameters
Bathymetry range	$0 \leq h \leq 16.54$ m
Porous layer thickness	$h_0 = 0.25$ m
Hydraulic conductivity	$\kappa = 3.162 \times 10^{-4}$
Drag coefficient	$c_d = 0.005$
Time increment	$\Delta t = 111.78$ s
Time steps per tidal period	400
Tidal periodicity	$T = 12.42$ h
Length of simulation	$0 \leq t \leq 6T$
Numerical implicity	$\theta = 1$
Number of nonlinear iterations	10

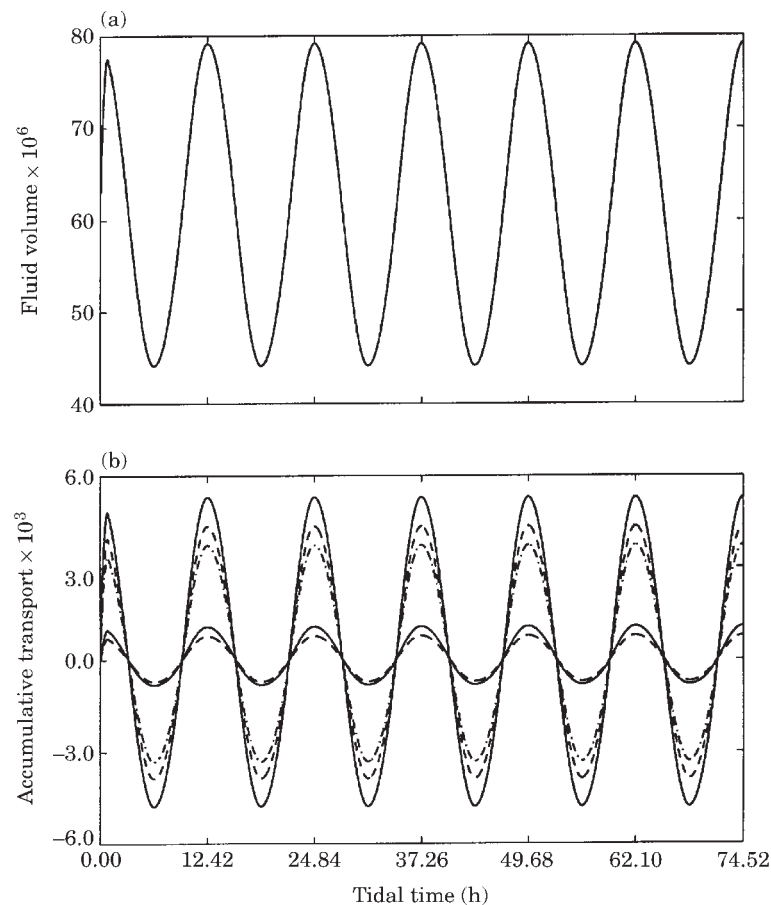


FIGURE 22. Time series of the total fluid volume (a) and the cumulative transport across the six transects (b) for the gtb9 grid. The group of periodic solid lines with higher amplitudes corresponds to the cumulative transport across the four transects across the central deep channel. The dotted and solid lines with much lower amplitudes are the cumulative transport across the two transects across the western and eastern lower bay tidal flats, respectively.

non-linear diffusion coefficient. A porous medium representation accounts for tidal flat drainage as the depth approaches small values comparable to the local sub-grid roughness. the model realistically simulates tidal flow allowing flooding and dewatering during flood and ebb stages. The two-dimensional model successfully reproduces identical results of a one-dimensional flooding and dewatering of a straight channel with uniformly sloping bathymetry. It also simulates rectangular channels with a linearly sloping bottom and with a V-shaped and an asymmetric W-shaped depth profile. The numerical solutions are smooth and physically consistent, and without any noticeable oscillation and distress in all the residual and transient analyses. Water is conserved throughout simulations.

Application to the Great Bay Estuary system shows very promising results despite the idealized porous substrate. Based on M_2 forcing, the residual bottom

stress is most intensified within the deep channel within the 5 m isobath, and the residual sediment transport is concentrated at the narrow strait connecting the northern channel and the lower bay. Further refinement of this simulation would require detailed description of the porous substrate and its variability, along with a similarly detailed description of the bottom stress coefficient.

Acknowledgements

The authors thank their colleagues Dr Rick Luettich Jr for helpful discussion; Dr Chris Naimie and Mr Jay Perry for assistance in mesh generation of the Great Bay mesh. Bathymetric data are provided by the Great Bay Estuarine Field Program under the New Hampshire Sea Grant College Program. Financial support from the National Science Foundation is gratefully acknowledged.

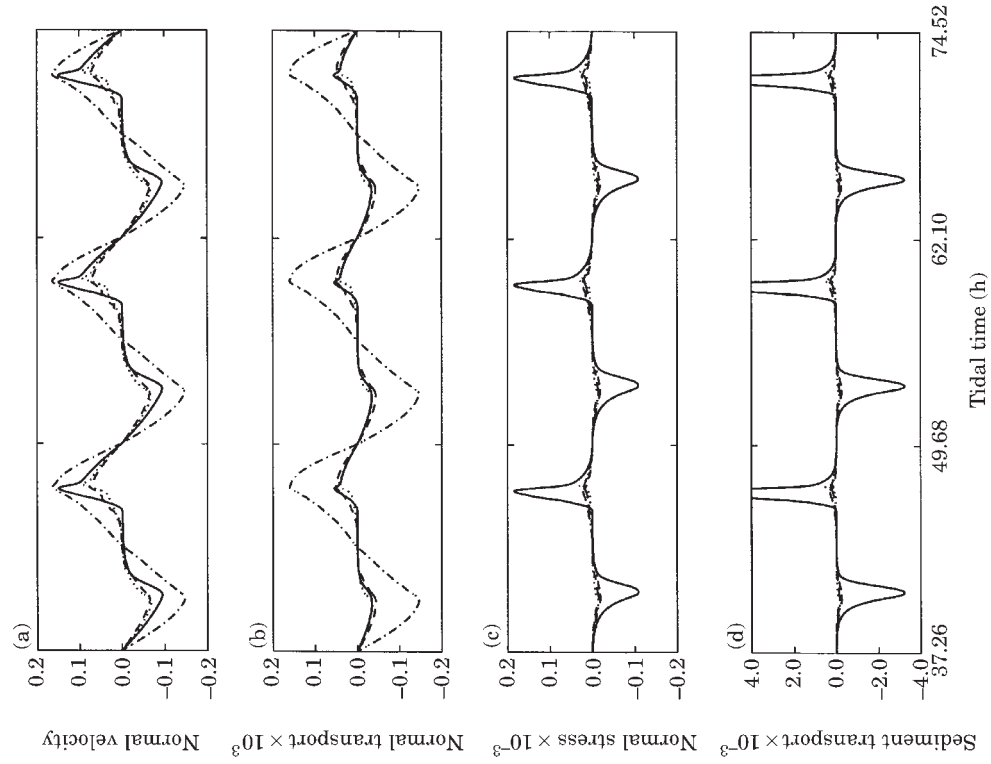


FIGURE 23. Time series of the maximum normal velocity (a), normal transport (b), maximum normal bottom stress (c) and maximum normal sediment transport across the five transects (d) during the second half of the gtb9 simulation (three M_2 periods). The periodic solid and dashed lines with higher amplitudes correspond to the results at the two end transects across the central deep channel. The much higher amplitude dashed line is the transect across the middle strait. The dotted and solid lines with much lower amplitudes are the results at the two transects across lower bay tidal flats.

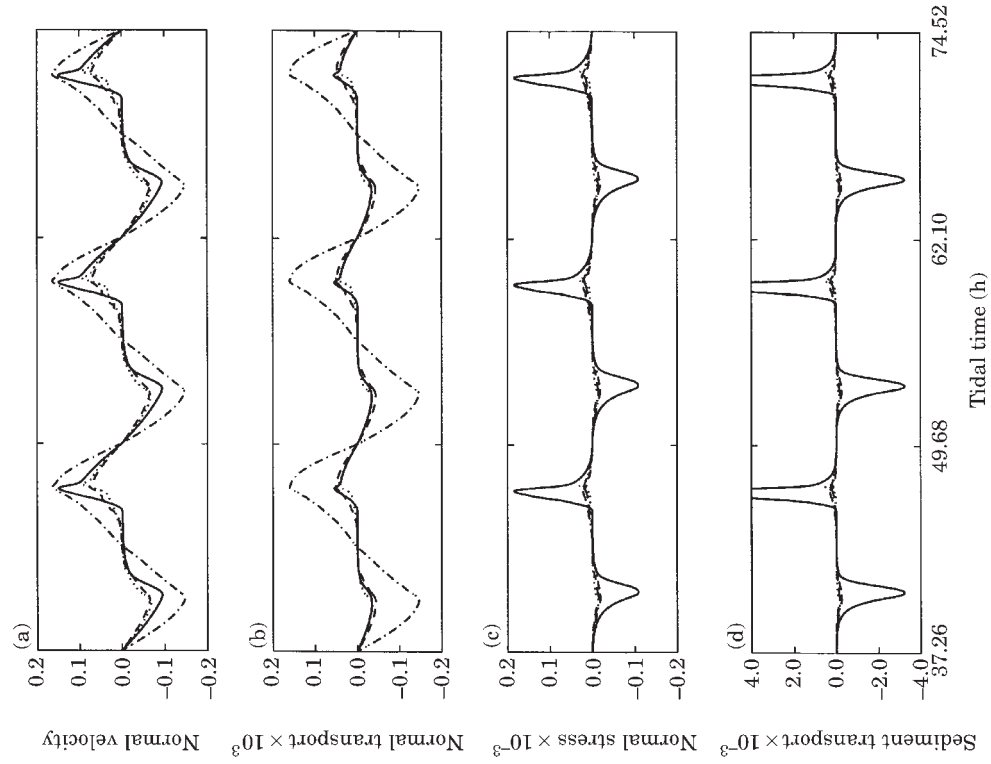


FIGURE 24. Time series of the maximum normal velocity (a), normal transport (b), maximum normal bottom stress (c) and maximum normal sediment transport (d) across the four transects at the south-eastern tidal flat in zoom window no. 3 during the second half of the gtb9 simulation (three M_2 periods). The periodic solid, dashed, dash-dotted and dotted lines correspond to the results at the transects going counterclockwise around the tidal flat respectively.

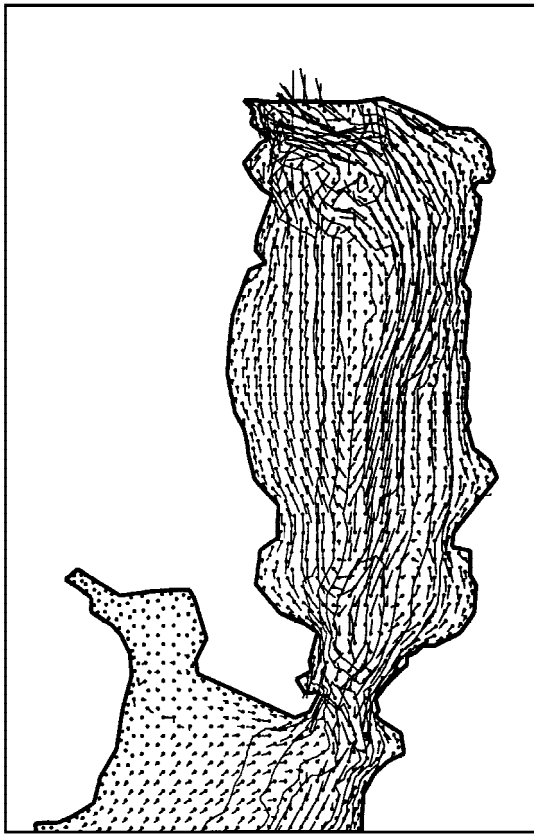


FIGURE 25. Residual transport of the upper Great Bay channel (gtb9, zoom window no. 1). The vectors are marked at their base and are drawn at the centroid of each element. The vectors are reduced by 50% for clarity.

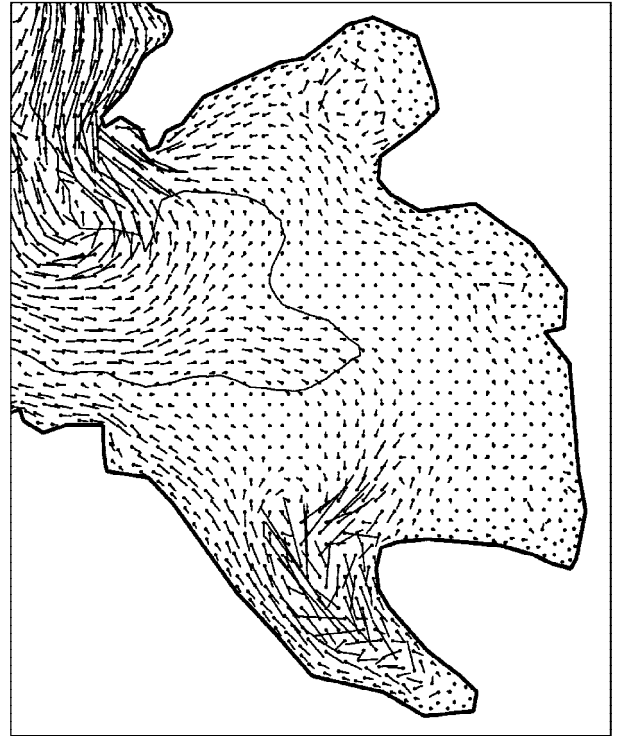


FIGURE 27. Residual transport of the lower eastern Great Bay tidal flats (gtb9, zoom window no. 3). The vectors are marked at their base and are drawn at the centroid of each element. The vectors are magnified five times.

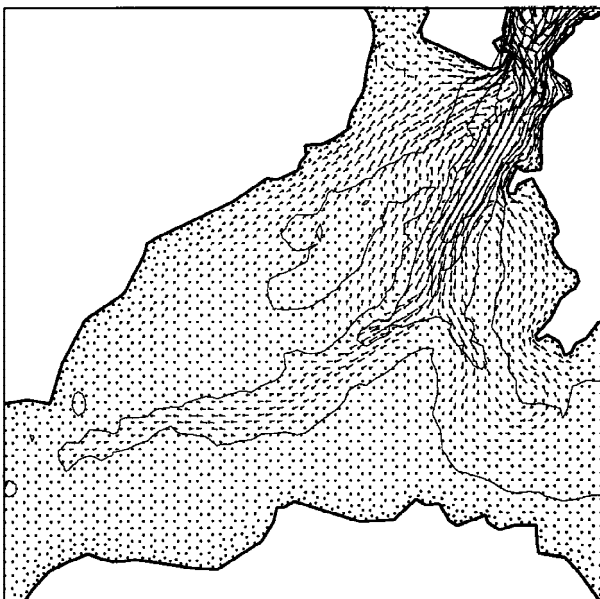


FIGURE 26. Residual transport of the lower Great Bay (gtb9, zoom window no. 2). The vectors are marked at their base and are drawn at the centroid of each element.

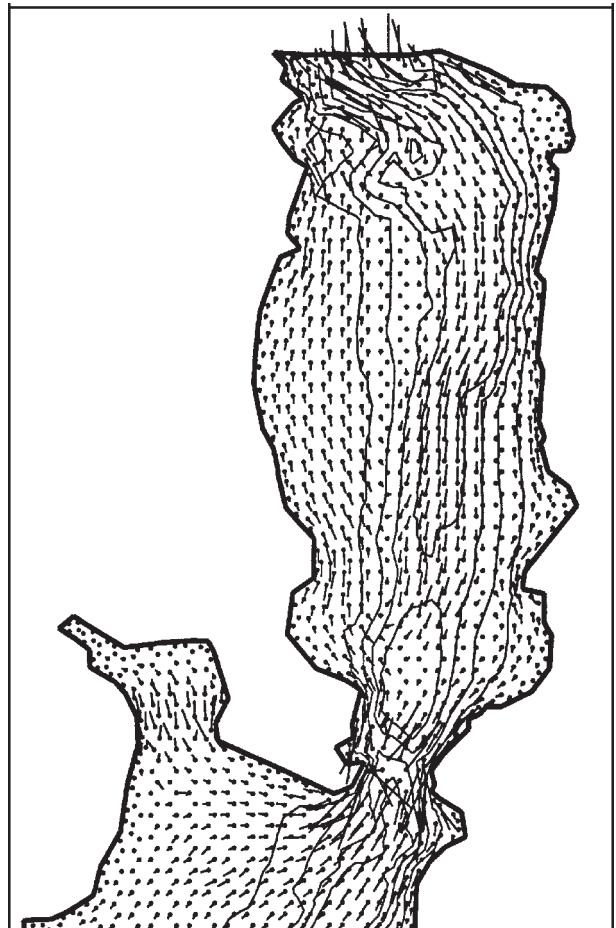


FIGURE 28. Residual bottom stress of the upper Great Bay channel (gtb9, zoom window no. 1).

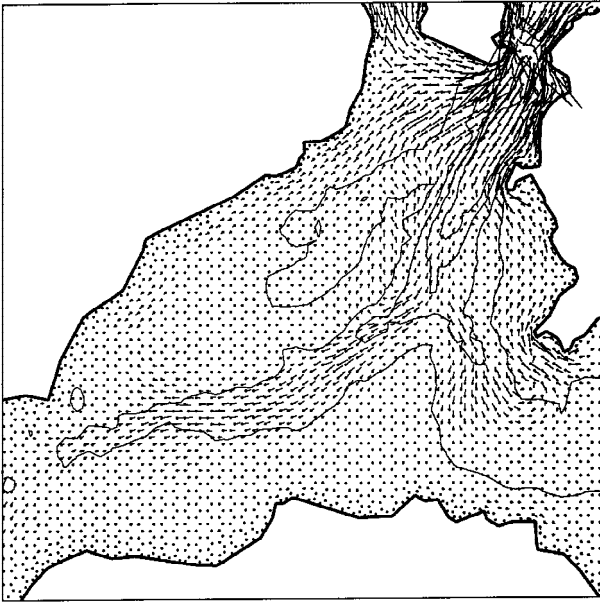


FIGURE 29. Residual bottom stress of the lower Great Bay (gtb9, zoom window no. 2).

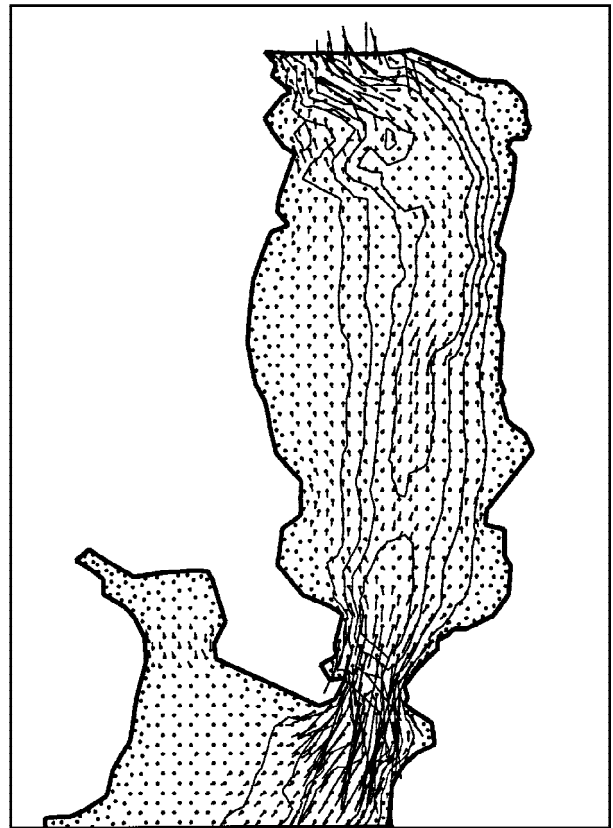


FIGURE 31. Residual sediment transport of the upper Great Bay channel (gtb9, zoom window no. 1).

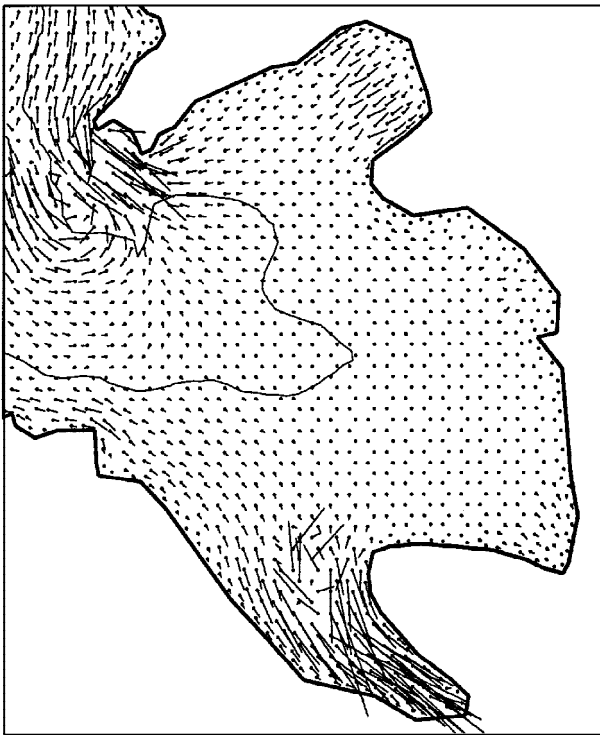


FIGURE 30. Residual bottom stress of the lower eastern Great Bay tidal flats (gtb9, zoom window no. 3).

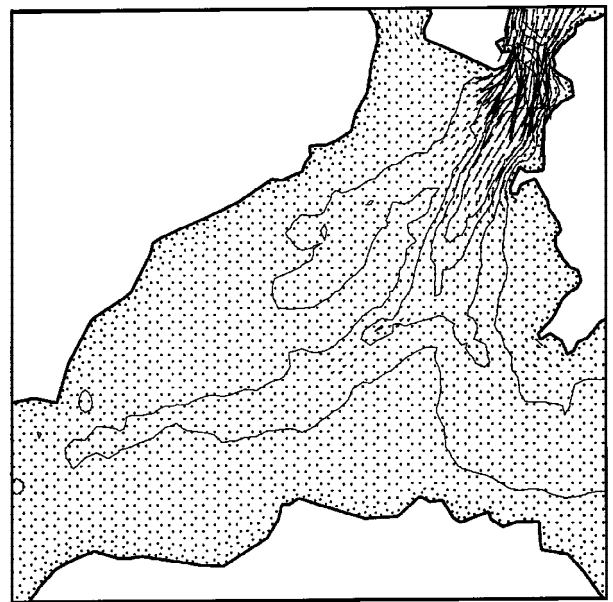


FIGURE 32. Residual sediment transport of the lower Great Bay (gtb9, zoom window no. 2).

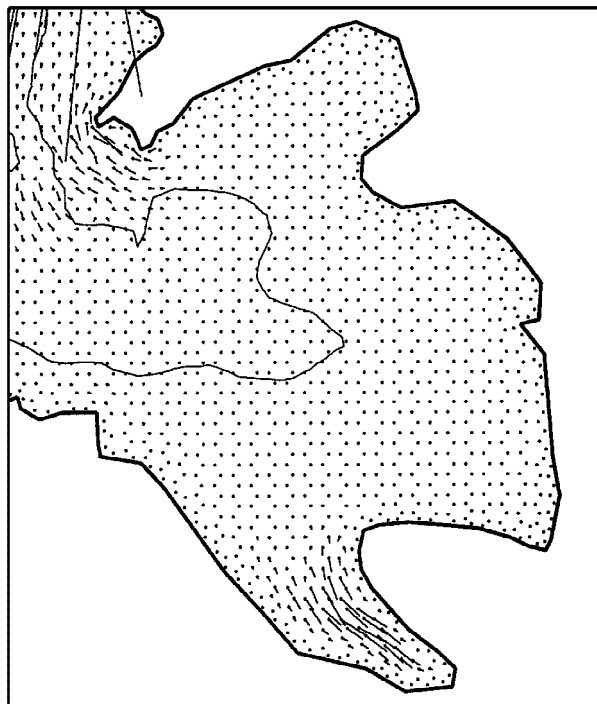


FIGURE 33. Residual sediment transport of the lower eastern Great Bay tidal flats (gtb9, zoom window no. 3).

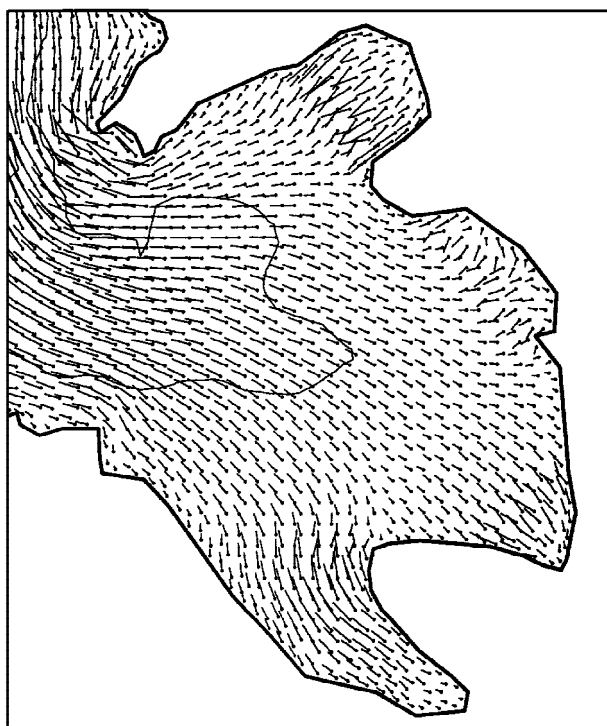


FIGURE 34. Circulation pattern of the lower eastern Great Bay tidal flats (gtb9, zoom window no. 3) at maximum ebb at time step no. 100.

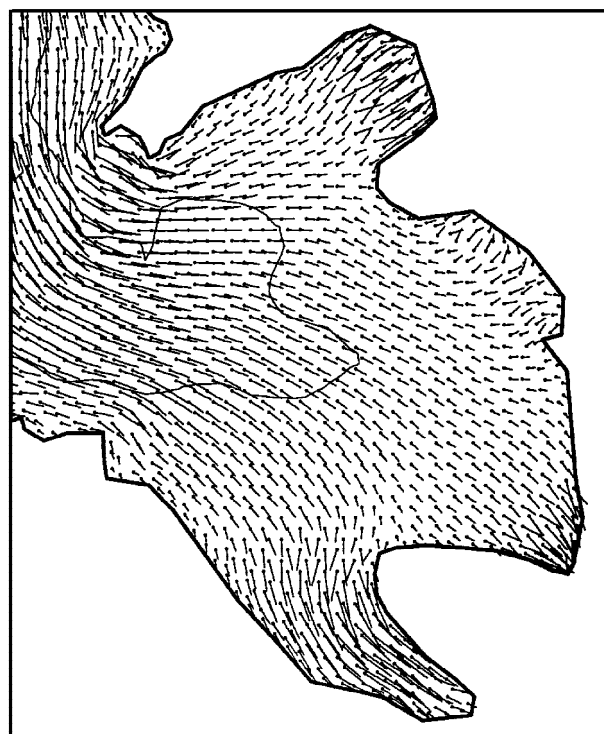


FIGURE 35. Circulation pattern of the lower eastern Great Bay tidal flats (gtb9, zoom window no. 3) at maximum flood at time step no. 315.

References

- Akanbi, A. A. & Katopodes, N. D. 1988 Model for flood propagation on initially dry land, ASCE. *Journal of Hydraulic Engineering* **114**, 689–706.
- Austria, P. M. & Aldama, A. A. 1990 Adaptive mesh scheme for free surface flows with moving boundaries. In *Computational Methods in Surface Hydrology* (Gambolati, G., Rinaldo, A., Brebbia, C. A., Gray, W. G. & Pinder, G. F., eds). Springer-Verlag, pp. 456–460.
- Cialone, J. 1991 *Coastal Modeling System (CMS) User's Manual, Instruction Report CERC-91-1*, Coastal Engineering Research Center, U.S. Army Engineer Waterways Experiment Station, Vicksburg, MS, U.S.A.
- Defina, A., D'Alpaos, L. & Maticchio, B. 1994 A new set of equations for very shallow water and partially dry areas suitable to 2d numerical models. In *Modelling of Flood Propagation Over Initially Dry Areas* (Molinari, P. & Natale, L. eds). ASCE, New York, NY, pp. 72–81.
- Flather, R. A. & Heaps, N. S. 1975 Tidal computations for Morecambe Bay. *Geophysical Journal of the Royal Astronomical Society* **42**, 489–517.
- Flather, R. A. & Hubbert, K. P. 1990 Tide and surge models for shallow water—Morecambe Bay revisited. In *Modeling Marine systems* (Davies, A. M., ed.). CRC Press Inc., Boca Raton, FL, pp. 135–166.
- Friedrichs, C. T. & Madsen, O. S. 1992 Nonlinear diffusion of the tidal signal in frictionally dominated embayments. *Journal of Geophysical Research* **97**, 5637–5650.
- Friedrichs, C. T., Lynch, D. R. & Aubrey, D. G. 1992 Velocity asymmetries in frictionally-dominated tidal embayments: longitudinal and lateral variability. In *Dynamics and Exchanges in Estuaries and the Coastal Zone, Coastal and Estuarine Studies* (Prandle, D., ed.) Vol. 40. AGU, Washington D.C., pp. 277–312.
- Hervouet, J.-M. & Janin, J.-M. 1994 Finite element algorithms for modelling flood propagation. In *Modelling of Flood Propagation Over Initially Dry Areas* (Molinari, P. & Natale, L., eds). ASCE, New York, NY, 102–113.
- Jelesnianski, C. P., Chen, J. & Shaffer, W. A. 1992 SLOSH: Sea, lake, and overland surges from hurricanes, *NOAA Technical Report NWS*, 48 pp.
- Katopodes, N. D. 1982 On zero-inertia and kinematic waves, *ASCE. Journal of Hydraulic Engineering* **108**, 1380–1387.
- Katopodes, N. D. 1984 Fourier analysis of dissipative FEM channel flow model, *ASCE. Journal of Hydraulic Engineering* **110**, 927–944.
- LeBlond P. H. 1978 On tidal propagation in shallow rivers. *Journal of Geophysical Research* **82**, 4717–4721.
- Leendertse, J. J. 1970 A water-quality simulation model for well-mixed estuaries and coastal seas: principles of computation, *Rand Corporation Report RM-6230-rc*, Vol. 1.
- Leendertse, J. J. 1987 Aspects of SIMSYS2D, a system for two-dimensional flow computation, *Rand Corporation Report R-3572-USGS*.
- Leenknecht, D. A., Earickson, J. A. & Butler, H. L. 1994 Numerical simulation of Oregon Inlet control structures' effects on storm and tide elevations in Pamlico Sound. In *Technical Report, CERC-84-2*, Coastal Engineering Research Center, U.S. Army Engineers Waterways Experiment Station, Vicksburg, MS.
- Lighthill, M. J. & Whitham, G. B. 1955 On kinematic waves: I-flood movement in long rivers. *Proceedings of the Royal Society London* **229**, 281–316.
- Liong, S. Y., Selvalingam, S. & Brady, D. K. 1989 Roughness values for overland flow in subcatchments, ASCE. *Journal of Irrigation Drainage Engineering* **115**, 204–214.
- Luettich, R. A., Jr & Westerink, J. J. 1995a An assessment of flooding and drying techniques for use in the ADCIRC hydrodynamic model, *Contractors Report, Contract No. DACW39-94-M-5869*, Coastal Engineering Research Center, U.S. Army Engineer Waterways Experiment Station, Vicksburg, MS.
- Luettich, R. A., Jr & Westerink, J. J. 1995b Implementation and testing of elemental flooding and drying in the ADCIRC hydrodynamic model, *Final Contractors Report, Contract No. DACW39-94-M-5869*, Coastal Engineering Research Center, U.S. Army Engineer Waterways Experiment Station, Vicksburg, MS.
- Lynch, D. R. & Gray, W. G. 1979 A wave equation model for finite element computations. *Computers & Fluids* **7**, 207–228.
- Lynch, D. R. & Gray, W. G. 1980 Finite element simulation of flow in deforming regions. *Journal of Computational Physics* **36**, 135–153.
- Murty, T. S. 1983 Diffusive kinematic waves versus hyperbolic long waves in tsunami propagation. In *Proceedings of the International Tsunami Symposium, August 1983, Hamburg* (Bernard E. N., ed.). pp. 1–22.
- Reid, R. O. & Bodine, B. R. 1968 Numerical model for storm surges in Galveston Bay. *Journal of the Waterways and Harbors Division* **94**, 33–57.
- Short, F. T. (ed.) 1992 *The Ecology of the Great Bay Estuary, New Hampshire and Maine: An Estuarine Profile and Bibliography*, NOAA—Coastal Ocean Program Publication.
- Sidén, G. L. D. & Lynch, D. R. 1988 Wave equation hydrodynamics on deforming elements. *International Journal for Numerical Methods in Fluids* **8**, 1071–1093.
- Sielecki, A. & Wurtele, M. G. 1970. The numerical integration of the nonlinear shallow-water equations with sloping boundaries. *Journal of Computational Physics* **6**, 219–236.
- Strelkoff, T. & Katopodes, N. D. 1977 Border irrigation hydraulics with zero-inertia, *ASCE. Journal of Irrigation and Drainage Engineering* **103**, 325–342.
- Swift, M. R. & Brown, W. S. 1983 Distribution of bottom stress and tidal energy dissipation in a well-mixed estuary. *Estuarine, Coastal and Shelf Science* **17**, 297–317.
- Thomas, W. A., McAnally, W. H., Jr & Letter J. V., Jr 1990 *Appendix F: User Instructions for RMA-2V, A Two-Dimensional Model for Free Surface Flows*, Draft copy.
- USACE 1981 *HEC-1 Flood Hydrograph Package*. U.S. Army Corps of Engineers, Hydrologic Engineering Center.
- Vemulakonda, S. R., Schenffner, N. W., Earickson, J. A. & Chou, L. W. 1988 Kings Bay coastal processes model, *Technical Report, CERC-88-3*, Coastal Engineering Research Center, U.S. Army Engineers Waterways Experiment Station, Vicksburg, MS.
- Wooding, R. A. 1965 A hydrologic model for the catchment-stream problem. I: Kinematic wave theory, *Journal of Hydrology* **3**.
- Yeh, G. T. & Chou, F. K. 1979 Moving boundary numerical surge model. *Journal of the Waterway, Port, Coastal and Ocean Division* **105**, 247–263.
- Yu, C. S., Fettweis, M., Rosswo, F. & Berlamont, J. 1990 A 2D model with changing land-water boundaries. In *Computational Methods in Surface Hydrology* (Gambolati, G., Rinaldo, A., Brebbia, C. A., Gray, W. G. & Pinder, G. F., eds). Springer-Verlag, pp. 456–460.